

Characterisation of Ga₃Ni₂ Surface Structure

Josh Cannon

201292953

Department of Physics, University of Liverpool

Supervisor: Dr Hem Raj Sharma

MPhys Project Thesis

May 17, 2022



Declaration of Authorship

I, Joshua Cannon, confirm that the work submitted in this thesis is my own, and that appropriate credit has been given where reference is made to the work of others.

Signature: _____

Date: _____

Acknowledgements

I would like to thank everybody in the surface science research group at Liverpool for their assistance with this project. In particular PhD students Oscar Shedwick, Amnah Alofi and Ahowd Alfahad for collecting the data analysed in this report, as well as for their advice. I wish them all the best of luck with their PhD studies.

I would like to extend my highest gratitude to Dr. Hem Raj Sharma, both for giving me the opportunity to work on this project and for his insights during the course of it. I wish him continued success in his career.

Finally, I would like to acknowledge students from the MPhys class of 2022 who helped make this degree a hugely enjoyable and fulfilling experience. Fred Downes, Ethan Hughes and in particular Brad Lewis, for whom I wish the utmost success in his upcoming PhD.

Abstract

A study of the surface atomic structure of some of the high symmetry lattice planes in the intermetallic compound Ga_3Ni_2 is presented. These are the (100), (010), (001) and $(2\bar{1}0)$ planes. Characterisation of surface structure was completed through analysis of data from low energy electron diffraction, scanning tunnelling microscopy and x-ray photoelectron spectroscopy experiments.

Contents

1	Introduction	6
1.1	Applications of Ga_3Ni_2	6
1.2	Production of Ga_3Ni_2	6
1.3	Crystal Lattices	7
1.4	Lattice Planes	7
1.5	Nature of Material Surfaces	8
2	Methods	12
2.1	Necessity of ultra high vacuum (UHV)	12
2.2	UHV chamber design	12
2.3	Reciprocal space	14
2.4	Sample preparation	15
2.5	Low energy electron diffraction (LEED)	16
2.5.1	Experimental Principle & Setup	16
2.6	Scanning tunnelling microscopy (STM)	17
2.6.1	Experimental Principle & Setup	17
2.7	X-ray photoelectron spectroscopy (XPS)	19
2.7.1	Experimental Principle & Setup	19
2.7.2	Methods of Analysis	23
3	Results and Discussions	25
3.1	XPS Results	25
4	References	27
5	Appendices	29
5.1	Appendix A: Bravais Lattices	29
5.2	Appendix B: Calculation of Miller Indices	30
5.3	Appendix C: Bulk Plane Structures	30
5.4	Appendix D: Physical Principles of Vacuum Pumps	31
5.5	Appendix E: The Piezoelectric Effect	35
5.6	Appendix F: K_α X-ray Sources	36
5.7	Appendix G: Summary of XPS Related Quantities	36

Chapter 1

Introduction

1.1 Applications of Ga₃Ni₂

The intermetallic alloy Ga₃Ni₂ has potential applications as a catalyst for the production of methanol from carbon dioxide. [1]. This process proceeds via the following reaction: $CO_2 + 3H_2 \rightarrow CH_3OH + H_2O$. This could prove to be a hugely important process in the future; both in terms of reducing atmospheric CO₂ emissions from industrial processes by finding a use for them, and in terms of producing methanol, which is an alternative fuel to petroleum products in internal combustion engines. In order to understand the catalytic behaviour of this material, it is important to understand the structure of its surface as best as possible. This is because it is the material surface to which carbon dioxide and hydrogen molecules are adsorbed, lowering the activation energy for the reaction and allowing it to proceed more readily. [2]. In order for a material surface to be fully characterised, four pieces of information are needed: the locations of atoms on the surface, the type of atoms on the surface, the chemical composition (ratio of different elements) of the surface and the strength of bonds, bond length and bond angles on the surface. No single experimental procedure is capable of returning information on all four aspects, so multiple techniques must be used for surface structure characterisation. Here, the techniques of low energy electron diffraction (LEED), scanning tunnelling microscopy (STM) and X-ray photoelectron spectroscopy were used.

1.2 Production of Ga₃Ni₂

For studies of the material surface at the atomic scale, only small crystals need to be produced, on the order of a few cm³. These can then be cut along specific crystallographic directions, in order to produce samples whose surface lies in a particular orientation. Growth of the larger sample was done via the Czochralski method [3]. This used a sample of pure Nickel as an initial *seed*, essentially a node around which nucleation of Ga₃Ni₂ can occur. This seed is immersed in a crucible containing Ga₇₅Ni₂₅ in the liquid phase, and is pulled out slowly whilst also being rotated at a constant rate. This encourages even growth of a sample of Ga₃Ni₂. The chamber containing the crucible and seed is evacuated to a pressure of 10⁻⁷ mbar, before being re-pressurised with pure Argon gas, to a pressure of 525 mbar. This mitigates the risk of surface contamination by gases such as Oxygen and Carbon.

This Ga_3Ni_2 sample is then cut into a wedge shape, along specific crystallographic directions. The wedge then becomes a seed itself for a second growth process.

An example of a Ga_3Ni_2 crystal grown by the Czochralski method is shown in *figure 1.1*



Figure 1.1: A single crystal sample of Ga_3Ni_2 grown via the Czochralski method. Note the rotational symmetry of the sample, generated by rotation of the seed at a constant rate during withdrawal from the crucible.

1.3 Crystal Lattices

The structure of Ga_3Ni_2 in its solid phase can be represented by a geometrical construction known as a *Bravais lattice*. This is a set of points, corresponding to positions of atoms, movements between which can be described by translation vectors: $\vec{T} = n_1\vec{a} + n_2\vec{b} + n_3\vec{c}$. The basis vectors \vec{a} , \vec{b} and \vec{c} are known as *primitive lattice vectors*, and whilst acting as basis vectors for a lattice, are not necessarily mutually perpendicular. Indeed, in the case of Ga_3Ni_2 \vec{a} and \vec{b} are not mutually perpendicular, and this is shown in *figure 1.2*. An important property of the Bravais lattice is that it will take on the same appearance when viewed from a particular direction, irrespective of the viewing position.

The simplest repeating unit of a Bravais lattice is known as a unit cell. There are fourteen distinct unit cells in three dimensions; a table of these can be found in *Appendix A: Bravais Lattices*. Any crystal can be considered as a combination of many of the same unit cell.

1.4 Lattice Planes

In an intermetallic compound such as Ga_3Ni_2 , a regular, periodic arrangement of all atom species is seen. This differs from more conventional alloys such as steels, where iron and carbon atoms are interspersed randomly (see *figure 1.3*). The crystal structure of Ga_3Ni_2 is shown in *figure 1.4*. Eight corners contribute $8 \times \frac{1}{8}$ Gallium atoms, plus two in the centre of the unit cell makes three. The two Nickel atoms in the centre result in the stoichiometric ratio being 3:2, and hence the chemical formula for the compound is Ga_3Ni_2 .

A key concept in crystal structures is that of *lattice planes*. These are 2 dimensional slices of the lattice, defined by a set of three numbers known as *Miller indices* (**hkl**).

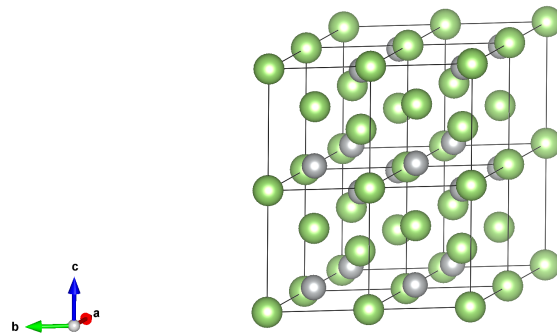


Figure 1.2: left: the primitive lattice vectors of Ga_3Ni_2 .

Figure 1.2: right: The Bravais lattice of Ga_3Ni_2 , with unit cells demarcated by black lines.

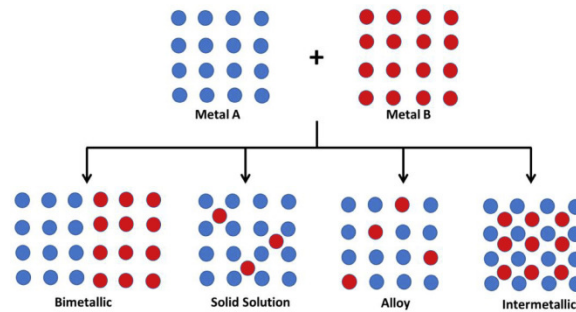


Figure 1.3: An diagram of the arrangement of atoms in different types of metallic compounds. Note the periodic arrangement of atom species in an intermetallic compound. [Credit - Marakatti, Peter (2018)].

An explanation of how the Miller indices are calculated for an arbitrary plane is given in *Appendix B: Calculation of Miller Indices*. Parallel planes will have the same atomic structures. Planes where all Miller indices are either one or zero are known as low index or *high symmetry* planes, whilst planes with one or more Miller indices greater than one are known as high index planes.

The surfaces of a crystal are also themselves lattice planes. However, they will not necessarily have the same atomic structures as parallel planes found in the bulk, (the bulk is the deep internal structure, well away from the surface).

The bulk structures of the lattice planes examined in this project can be found in *Appendix C: Bulk Plane Structures*.

1.5 Nature of Material Surfaces

The structure of a lattice plane on the surface of a crystal may be physically different to the structure of an equivalent plane in the bulk of the material. This is because atoms at the surface have fewer nearest neighbours, and therefore fewer bonding opportunities, than their bulk counterparts. (The number of nearest neighbours an atom has can also be referred to

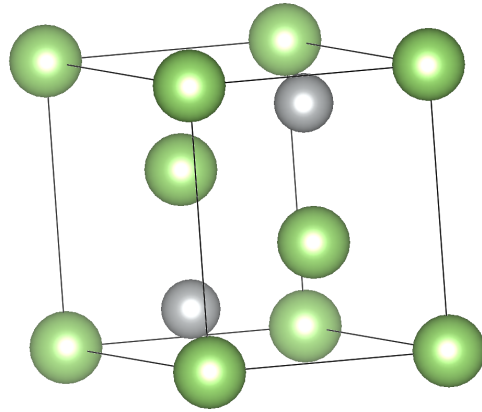


Figure 1.4: The unit cell of the Ga_3Ni_2 lattice. Gallium atoms are in green and Nickel in grey. [VESTA - Ocar Shedwick].

as the atom's *coordination number*). These so called 'dangling bonds' raise the energy of the surface of the material relative to the bulk. Surface atoms will try to compensate for this by rearranging their positions, with two common mechanisms being surface reconstruction and surface relaxation. An example of surface reconstruction is seen on the (110) surface of gold, and this is illustrated in *figure 1.5*. In this case, sets of three atomic rows have been removed, and this results in the generation of small (111) planes, known as *microfacets*. The (111) lattice plane is the plane with the lowest surface energy, and so the surface energy of the reconstructed (110) plane is lower than the original (110) plane.

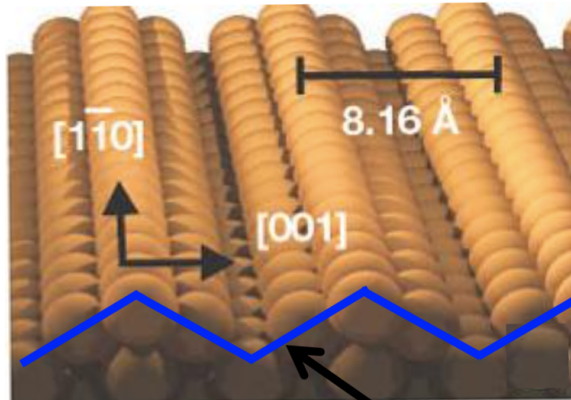


Figure 1.5: Illustration of surface reconstruction on the (110) surface of gold.

Surface reconstruction can also take place via the movement of atoms parallel to the plane of the surface. A good example of this is seen in the high symmetry surface planes of group IV elements, where atoms move parallel to the plane of the surface to form structures known as *dimers*. *Figure 1.6* shows the (100) surface of Silicon prior to reconstruction, with the topmost layer of atoms highlighted in orange. It can be seen that atoms in the bulk

form four covalent bonds to other Silicon atoms, whilst atoms on the surface form only two. The bonding on a particular row of surface layer silicon atoms is shown by the black line. Movement of atoms follows the red arrows; adjacent rows will move closer to one another, in order to open up a further bonding opportunity. *Figure 1.7* shows the same (100) surface after reconstruction. Rows of atoms in the topmost layer have moved closer to one another, forming dimers. Each silicon atom in the topmost layer now forms three covalent bonds, meaning only one, rather than two, is left 'dangling'. This reduces the surface energy of the (100) surface.

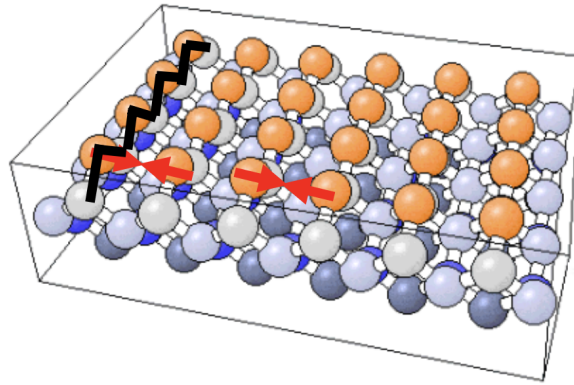


Figure 1.6: (100) surface of Silicon prior to dimerization. Orange topmost atoms form two bonds.

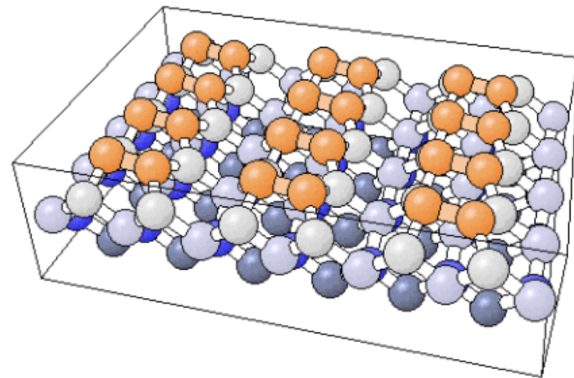


Figure 1.7: (100) surface of Silicon after dimerization has taken place. Orange topmost atoms now form three bonds.

In the surface relaxation mechanism, the topmost layer of atoms compresses into the layer below. This increases the coordination number of the topmost atoms, and hence results in a reduction in the energy of the material surface. This alone would also increase the coordination number of the second layer of atoms, and so the third layer will pull away from the second layer to compensate. This oscillation in layer separation can penetrate up to five or six layers into the material, and this region of layer spacing oscillation is known

as the *selvedge*. *Figure 1.8* shows how oscillation in layer spacing can penetrate multiple layers into the material.

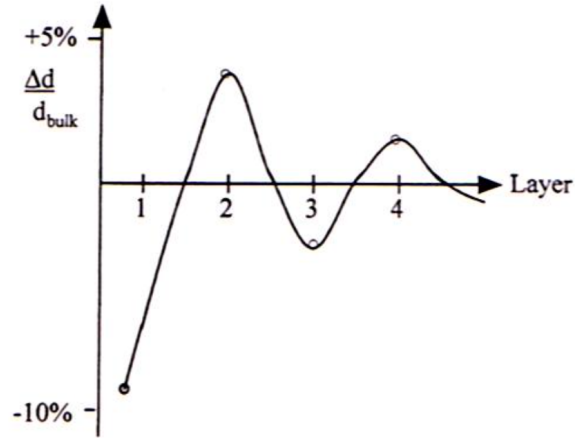


Figure 1.8: Plot of change in layer spacing vs. layer number. Δd is the difference between the layer spacing seen at the respective layer, and the nominal layer spacing seen deep in the material d_{bulk} .

Another structure which is often seen on crystal surface planes is the *step-terrace* structure. A lattice plane which appears to be flat when viewed at a large scale may actually be made up of several smaller planes (with the same miller indices), known as terraces, separated by vertical or near-vertical steps of atomic height. A schematic of this structure is shown in *figure 1.9*. The step - terrace structure is potentially beneficial for the catalytic properties of the material, as the step-terrace interface is often a preferred adsorption site for molecules [4].

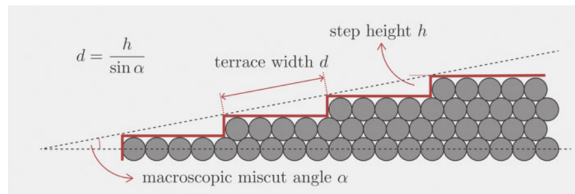


Figure 1.9: Illustration of the step - terrace structure seen on an arbitrary lattice plane. The normal vector to this plane will differ slightly from the normal vector to each individual terrace

Chapter 2

Methods

2.1 Necessity of ultra high vacuum (UHV)

If surface science experiments are to yield accurate information on the structure of materials at the atomic scale, they must be performed under ultra high vacuum conditions. Ultra high vacuum is generally accepted to be a pressure of around 10^{-10} Torr or lower [5] (1 Torr = 133.32 Pa = $\frac{1}{760}$ Atm = 0.75 mbar). There are two reasons for this: Firstly, many clean surfaces will very quickly become contaminated by ambient gases at atmospheric pressure, via the process of adsorption. This results in experiments yielding information about the lattice structure of atoms and molecules adsorbed to the surface, rather than the pure material surface itself. The set of points on a material surface corresponding to sites where molecules have been adsorbed is called the *superlattice*, and can exhibit different periodicity to the substrate lattice. This constitutes a problem for LEED experiments, as Bragg diffraction from atoms in the superlattice will contribute diffraction spots to the overall diffraction pattern.

Second, reducing pressure by reducing the number of gas molecules in the system, the mean free path λ of experimental probes (electrons and x-ray photons) is increased.

Example - Electrons in LEED: If λ can be made much greater than the distance electrons must travel from the filament, to the sample and back to the detector screen, then the probability of it interacting with a gas molecule will be very low. Interaction when the electron is travelling between the filament and the sample would alter its momentum, therefore changing its de Broglie wavelength according to $\lambda' = \frac{h}{p}$ (note λ' is used here to represent de Broglie wavelength, whereas λ indicates mean free path). A change to the de Broglie wavelength would in turn affect its diffraction behaviour, since diffraction from a crystal lattice is governed by Bragg's law; $2d\sin\theta = n\lambda'$. Interaction when the electron is travelling between

2.2 UHV chamber design

An example of a UHV system is shown in *figure 2.1*. It features two main chambers, each of which is surrounded with apparatus such as sputtering anodes, and electron guns for electron diffraction experiments. Manipulation instruments such as magnets allow the sample to be moved between chambers remotely. The red arrow indicates a linelock, this feature allows a

sample to be transferred from the lab into the chamber, without the entire system having to be at atmospheric pressure. It is effectively a smaller vacuum chamber, allowing evacuation and re-pressurisation to be done on a much shorter timescale than the main chamber itself. The linelock is isolated from the main chamber and a sample placed inside. It is then evacuated to the same pressure as the main chamber, and the seal lifted. The sample can then be moved into position in the main chamber via a sliding magnetic collar around the linelock.



Figure 2.1: An example UHV chamber. Linelock indicated by red arrow

UHV chambers are built from stainless steel, which is chosen for its good resistance to corrosion. Steel also has a low rate of outgassing; another useful property. Outgassing is the process by which molecules trapped within the bulk of a material diffuse to the surface and move out. In a UHV system, outgassed molecules could be adsorbed to the sample surface, which is manifestly undesirable. Degassing occurs for molecules which have been *absorbed* by a material, whereas *adsorption* refers to molecules which are attached to a material surface, rather than residing in the bulk. Adsorption can occur by two mechanisms: *chemisorption* is where atoms or molecules are affixed to a surface by chemical bonds, whilst *physisorption* is where the attraction between molecules and the surface is primarily due to Van der Waals forces [6].

Therefore, when preparing a UHV system, one must seek to remove not only atomic and molecular gases roaming freely within the chamber, but also gas molecules which have been adsorbed to internal surfaces, as reduced pressures may encourage their desorption.

No single pump is capable of taking a vacuum system from atmospheric pressure to 10^{-10} Torr. Instead, a series of pumps acts as a 'pressure ladder', to take the pressure inside the chamber down to the UHV regime (see *figure 2.2*). Numerous different types of pump can be used at each stage of this pressure ladder. The working principles of each type referenced here can be found in *Appendix D: Physical Principles of Vacuum Pumps*.

The first stage of depressurisation is known as 'roughening' and involves going from atmospheric pressure to 10^{-4} mbar. This is usually done by either a rotary pump or a sorption pump.

Once this pressure is reached, a second pumping stage will begin, usually performed by a diffusion or turbomolecular pump. The outlets of these pumps are connected to a rotary or sorption pump to improve their effectiveness. Turbomolecular pumps can operate in the

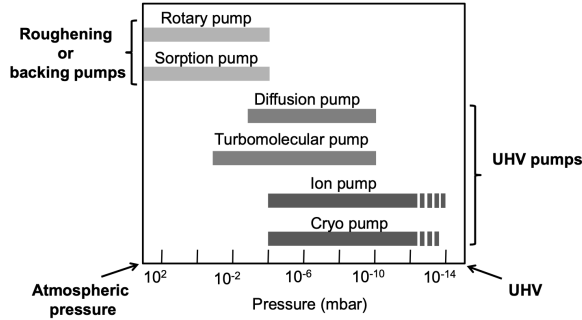


Figure 2.2: Operating pressures of various vacuum pumps

range $10^{-10} < P < 10^{-3}$ mbar, whilst diffusion pumps can operate in the range $10^{-10} < P < 0.1$ mbar. These pumps are classed as UHV pumps, since they are capable of reaching UHV pressures. If it is necessary for the chamber to be depressurised further, for example if an experiment is to take place over a period of time greater than 10^4 s, then ion or cryo pumps can be used. Ion pumps are capable of reaching pressures as low as 10^{-11} mbar [7].

An important part of UHV chamber preparation is *baking*. Whilst the pumping process removes free molecules in the chamber, it is also important to maximise the desorption of molecules adsorbed to internal surfaces in the chamber, so that they can be pumped out prior to the sample being put in. By heating the chamber to between 300 and 400°C, desorption of molecules from the internal chamber wall is promoted.

2.3 Reciprocal space

The Bravais lattice which describes the structure of crystals, including Ga_3Ni_2 , exists in *real space*. This is a vector space with which we are intimately familiar, and any vector in this space, including the translation vectors of Bravais lattices, can be described as a linear combination of three cartesian basis vectors; \hat{x} , \hat{y} and \hat{z} . This means that real vector space is three dimensional.

Associated with any Bravais lattice is a *reciprocal lattice*. This exists in a different vector space to real space, known as *reciprocal space*. Just as translation between any two points in the Bravais lattice can be described by a linear combination of primitive lattice vectors \vec{a} , \vec{b} and \vec{c} , basis vectors \vec{a}^* , \vec{b}^* and \vec{c}^* exist for the reciprocal lattice, and movement between points in reciprocal space can be expressed mathematically as a combination of these reciprocal lattice vectors.

$$\vec{a}^* = 2\pi \frac{\vec{b} \times \vec{c}}{\vec{a} \cdot \vec{b} \times \vec{c}}$$

$$\vec{b}^* = 2\pi \frac{\vec{c} \times \vec{a}}{\vec{a} \cdot \vec{b} \times \vec{c}}$$

$$\vec{c}^* = 2\pi \frac{\vec{a} \times \vec{b}}{\vec{a} \cdot \vec{b} \times \vec{c}}$$

Reciprocal lattice vectors, and indeed any distance in reciprocal space, will have dimensions length^{-1} .

Reciprocal and real space lattices are also the Fourier transforms of one another.

2.4 Sample preparation

A sample of Ga_3Ni_2 , cut so that the upward surface is a (010) plane, is shown in *figure 2.3*. Visibly, one can see that it appears clean and defect free, at least on a macroscopic level. However since it is exposed to air in the lab environment, the surface will be contaminated. Contamination consists of ambient gas molecules which are physisorped to the surface, as well as oxides and carbides formed by the chemisorption of gas molecules to the surface. Gallium Oxide (Ga_2O_3) and Nickel Oxide (NiO) are the pre eminent surface contaminants, as the rate of reaction between Gallium and Oxygen, and Nickel and Oxygen, is faster than with other contaminants. Before surface science experiments are performed, these contaminants must be removed.



Figure 2.3: A (010) sample of Ga_3Ni_2 (shiny material) spot welded to a mounting plate (silver, scratched material), which allows it to be moved without being directly touched.

The first stage of cleaning is washing with methanol, and this is done before the sample is placed into the vacuum chamber.

The sample is then placed into the chamber, via the load lock, and the process of **sputter-annealing** begins.

Sputtering involves bombarding the surface of the material with argon ions, in order to physically knock off contaminants. Naturally, this process removes not only contaminants but also native Gallium and Nickel atoms from the surface, creating defects. Some atom species will be more susceptible to removal through sputtering, either because they are bonded less tightly to the surface than other species, or they have a lower atomic weight than other species, meaning less force is required to physically move them. Sputtering should therefore be followed by a process of annealing in order to rectify the structure of the surface.

Annealing involves heating the sample (below the sample melting point) in order to increase the rate of diffusion of atoms within the material. Diffusion follows a concentration gradient, and so with a greater concentration of vacancies at the surface of the material than in the bulk, vacancies will diffuse away from the surface into the bulk. This can equivalently be viewed as bulk atoms diffusing to the surface, filling vacancies and effectively repairing the surface.

Another undesirable consequence of the sputtering process is the deposition and embedding of argon ions on to and into the material surface [8].

The sputter-anneal cycle should be repeated multiple times, in order to maximise the removal of contaminants and correction of surface defects.

2.5 Low energy electron diffraction (LEED)

2.5.1 Experimental Principle & Setup

Low energy electron diffraction exploits the wave-like properties of electrons, and the phenomenon of Bragg diffraction, to probe the symmetry and uniformity of material surfaces at the atomic level.

According to de Broglie's postulate, any particle with linear momentum (such as an electron in this case) is also a wave, with wavelength inversely proportional to its momentum; $\lambda = \frac{h}{p}$ [9].

When an electron de Broglie wave is incident on a crystal lattice, it will be reflected from lattice planes. When reflected waves meet each other they can interfere either constructively, (if their path difference is an even multiple of π), or destructively (if their path difference is an odd multiple of π). Geometrically one can derive the *Bragg condition* (see figure 2.4), which states that if constructive interference occurs for waves reflected from successive lattice planes, then the relationship $2d\sin\theta = n\lambda$ must be satisfied [10]. This means that constructive interference of electron wave functions will only occur at certain angles of reflection.

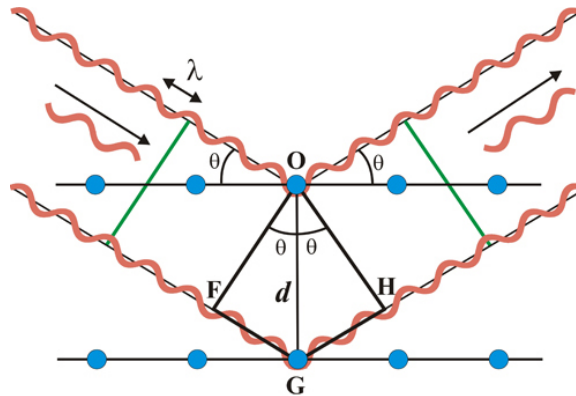


Figure 2.4: Geometrical derivation of the Bragg condition. Note that the two reflected waves are in phase, their crests and troughs line up as indicated by the green line. The additional distance travelled by the lower wave is $2 \times d\sin\theta$.

A schematic of a typical LEED setup is shown in *figure 2.5*. Electrons emitted via thermionic emission are accelerated to a uniform kinetic energy (and therefore a uniform de Broglie wavelength) before impacting on the sample. Some electrons are elastically scattered (reflected) in certain directions θ according to the Bragg condition, whilst some electrons are inelastically scattered from the negative charge density around individual atoms. Back scattered electrons are directed towards a fluorescent screen, which is held at a positive voltage in order to accelerate electrons into it, providing them with sufficient kinetic energy to cause light emission upon impact. A *suppressor voltage* is applied to grids between the sample and the screen, which filters out lower energy inelastically scattered electrons, preventing them from hitting the screen.

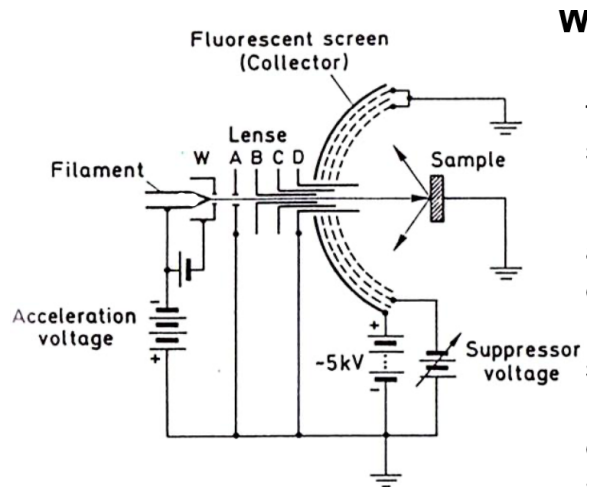


Figure 2.5: Illustration of a LEED setup

If the sample of the surface is sufficiently clean and defect free, the image on the fluorescent screen will be a series of bright spots (corresponding to reflection angles where constructive interference occurs) on a dark background. This image is not an image of the Bravais lattice of the sample, rather it is the *reciprocal lattice* which is seen.

Analysis of LEED images allows the symmetry of the unit cell to be examined, and if one is able to transform between reciprocal and real space distances, the dimensions of the unit cell can also be calculated.

2.6 Scanning tunnelling microscopy (STM)

2.6.1 Experimental Principle & Setup

STM uses the phenomenon of quantum tunnelling to probe the topography of material surfaces. Unlike LEED, the images returned by this technique reflect the structure of the surface in real space.

Particles governed by quantum mechanics are capable of passing through potential barriers, a phenomenon known as quantum tunnelling which is not predicted by classical physics. A particle wave function in a spatial region containing a potential barrier has an exponential

component inside the barrier, and a lower amplitude, sinusoidal component on the far side of the barrier. The extent of amplitude loss between the near and far sides of the barrier is governed by its depth, and the rate of decay of the exponential function. This scenario is counterintuitive, one would predict that the complex amplitude of the wave function should be zero both inside and on the far side of the barrier.

In the case of electrons, an electron in a conducting material has a wave function which can penetrate across a dielectric region to a conducting region on the other side. This can be interpreted as a current flowing through the classically forbidden dielectric region, with the magnitude of this tunnelling current inversely proportional to the width of the barrier.

The process of STM involves bringing an atomically sharp conducting tip close to a conducting material. This induces tunnelling of electrons between conduction band states in the sample, and conduction band states in the tip. Because the tunnelling probability is equal for tunnelling in either direction, a slight potential difference is maintained between the tip and the sample in order to ensure a tunnelling current flows in one direction only. Since the strength of this tunnelling current is related to the distance between the tip and the sample ($I_t \propto e^{-kd}$), moving the tip in the $x-y$ plane, and measuring the resulting tunnelling current, allows the height z of the material to be derived. In this way, a 3D image of the material surface can be constructed. In STM operation two images are produced: a forward scanned image and a backward scanned image. To obtain a backward scanned image, the direction of tip motion in the $x-y$ plane is reversed relative to the forward image.

If the surface of the sample is sufficiently clean, care is taken to eliminate sources of vibration in the setup as best as possible, and the STM tip is atomically sharp, individual atoms and the spaces between them can be seen in STM images. It is important that the tip be atomically sharp because this ensures the tunnelling distance only depends on the height of the surface, and not to which particular atom in the tip electrons are tunnelling from / to. The STM tip must also be *symmetrical*; any asymmetry will result in the forward scanned and backward scanned images appearing different.

Figure 2.6 is a photograph of the STM apparatus used to collect the data discussed further on in this report.

The scanning tunnelling microscope can be operated in one of two modes:

Constant current mode involves adjusting the position of the tip in the z axis, in order to keep the tunnelling current constant as the tip is moved through x and y . Vertical movement of the tip therefore directly reflects the vertical morphology of the material surface. Operation in this mode requires a high-frequency feedback loop; the tunnelling current must be measured, and the height of the tip above the surface altered to restore the strength of the tunnelling current to a reference value, before the tip is moved to a new position in the $x-y$ plane. Lateral movement of the tip over atomic-sized distances is possible thanks to piezoelectric components (see *Appendix E: The Piezoelectric effect*). Since the tunnelling current at a particular point above the surface is unknown until the tip is actually moved above said point, operation of the STM in this mode carries the risk of the tip making contact with major prominences on the surface. This would spoil the atomic sharpness of the tip, and therefore reduce the image quality.

Constant height mode involves keeping the z position of the tip constant, and measuring the tunnelling current at different points in the $x-y$ plane. This position can be chosen so as to mitigate the risk of the tip crashing into major prominences on the surface. The inherent risk associated with this mode of operation is that the surface drops too low, and the tunnelling current becomes too small to detect. However since this is preferable to ruining the tip, constant height mode is the mode a scanning tunnelling microscope is

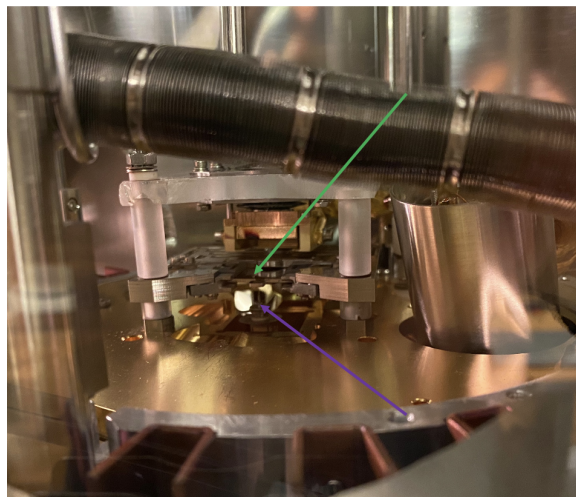


Figure 2.6: STM apparatus through a viewing port on a UHV chamber. The sample is mounted upside down, and is indicated by the green arrow. The STM tip is barely visible, but is indicated by the purple arrow. The whole setup is mounted on magnets, rather than being directly affixed to the chamber itself, in order to isolate it from vibration which can produce *noise* in the resulting image.

typically operated in.

2.7 X-ray photoelectron spectroscopy (XPS)

2.7.1 Experimental Principle & Setup

Unlike LEED and STM, XPS does not provide one with a visual representation of a material surface. Rather, XPS probes the type of atoms on the surface. By looking at the concentrations of different atom types, the surface's *chemical composition* can be determined.

The principle behind XPS is the photoelectric effect. This is the emission of electrons from core energy levels in atoms, induced by the absorption of a photon (photons in XPS are in the X-ray energy range). This photon must supply the electron with sufficient energy for it to overcome the electrostatic attraction to the atomic nucleus; this is known as the *binding energy* and is unique to each element (and also to the atomic orbital the electron originates from). Photon energy is given by $E = h\nu$, where h is Planck's constant and ν is the frequency of the photon. Energy supplied to an electron will first go into overcoming binding energy, but any excess will become the kinetic energy of the emitted electron. The kinetic energy of an emitted electron can therefore be expressed as $E_k = h\nu - E_B$. However, a further consideration must be made: because photoelectrons can be emitted from atoms a few layers below the surface of the material, for electrons to be truly 'emitted' (i.e. leave the material itself, so that their kinetic energy is actually measurable), the attenuation of their kinetic energy as they make their way through the material, to the surface, must be taken into account. This consideration manifests itself in the parameter *work function*, ϕ . ϕ is the kinetic energy loss which is incurred by a photoelectron in order for it to leave the

material surface. Therefore the kinetic energy of a photoelectron is $E_k = h\nu - E_B - \phi$. If the value of ϕ for the material being studied is known, along with the photon frequency, then a measurement of electron kinetic energy allows the binding energy of the atom which emission occurred from to be determined. Since binding energies for orbitals in different elements are established, tabulated values, the species of atom which emission occurred from can be derived.

The source itself must be electrically grounded, as emission of photoelectrons from an electrically isolated sample would cause the sample to become positively charged, in turn raising the binding energy for core level electrons.

To maximise the accuracy of XPS experiments, photons causing emission should be as close to monochromatic as possible. The standard X-ray source has a water cooled Al/Mg twin anode held at a potential of ~ 15 KeV onto which electrons are focused from a filament. The high energy electrons eject electrons from the core levels of the atoms in the anode. When these core levels decay they give rise to fluorescence x-rays with energies and line widths that are characteristic of the element. Aluminium and Magnesium anodes are chosen because the characteristic K_α x-rays from these sources are around 1eV in width. (Details of the K_α emission from these sources can be found in *appendix F: K_α X-ray sources*). A higher resolution can be achieved by passing x-rays through a diffraction grating, but this increase in resolution comes at the cost of a decrease in intensity, necessitating a longer time period for data acquisition.

The key aspect of XPS is accurate measurement of the photoelectron kinetic energy distribution (number of electrons detected as a function of their kinetic energy). The instrument responsible for this is the *hemispherical analyser* (see *figure 2.7*).

The hemispherical analyser consists of three parts; an **electron lens system**, two **concentric hemispheres** and an **electron multiplier detector**.

The **electron lens system** collimates emitted photoelectrons so that they will all be following the same initial trajectory when they pass through the opening aperture and into the void between the concentric hemispheres.

The **concentric hemispheres** are responsible for filtering electrons of different kinetic energies, so that only one particular energy is allowed to reach the detector at any one time. This particular energy is known as the pass energy of the detector. Energy filtering is achieved by holding the outer hemisphere at a negative potential, and the inner hemisphere at a positive potential. Electrons are directed through the opening aperture, and into the void between the two hemispheres. The electric field in this region pulls electrons towards the inner hemisphere, however since the electron is moving forwards with some velocity, and the hemisphere it is attracted to curves away from the trajectory of the electron, the electron will follow a circular path between the two hemispheres. This is analogous to the motion of a body in a gravitational orbit; with sufficient velocity tangential to the gravitational force acting on it, the body will orbit at a constant radius. By tuning the electric potentials of the two hemispheres, one can effectively specify what velocity electrons must have in order to make it all the way through the void, to the detector. Since velocity is related to kinetic energy through $E_k = \frac{1}{2}mv^2$, this allows only electrons of a specific kinetic energy to reach the detector. Electrons with kinetic energy, and hence velocity, which is too low will impact upon the surface of the inner hemisphere, and electrons with kinetic energy and velocity which is too high will impact upon the surface of the outer hemisphere. In either case, these electrons will not reach the detector.

The **electron multiplier detector** relies on the phenomenon of secondary emission,

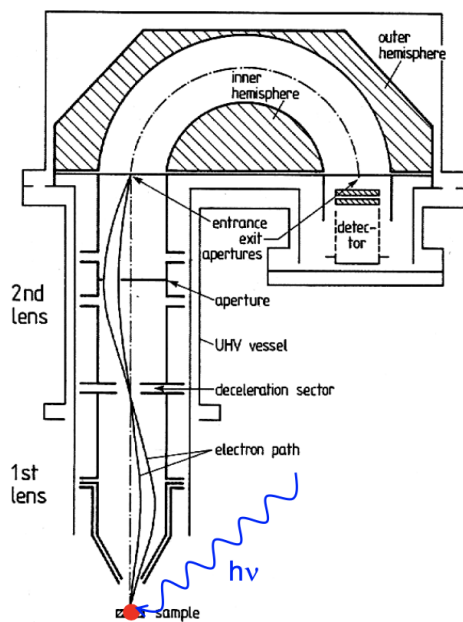


Figure 2.7: The hemispherical analyser setup

in order to increase the detectability of electrons which have passed between the concentric hemispheres. Secondary emission is a process whereby an electron incident on a secondary emissive material can induce emission of more than one electron.

A type of electron multiplier known as a discrete dynode is shown in *figure 2.8*. An electron entering the detector impacts upon a plate, which is held at a positive potential so that the electron is accelerated into it. This increases the kinetic energy of the electron before the collision, resulting in the collision being sufficiently energetic for more than a single electron to be released from the material. These emitted electrons are then accelerated into a subsequent plate, held at a larger positive potential than the first. This collision induces emission of more electrons (a greater number than the number of electrons incident), and this process repeats several times along the length of the multiplier tube. This results in a cascade of electrons reaching the detector, inducing a current pulse. The kinetic energy of the electron which originally entered the multiplier tube can be reconstructed from the height of this pulse, since a greater initial E_k will result in the eventual cascade containing more electrons.

If the potential difference between the two concentric hemispheres is increased at a constant rate, the pass energy of the system will also increase at a constant rate. This means that the number of electrons reaching the detector per second will be the same at all kinetic energies.

The output of an XPS experiment is a spectrum showing the intensity of electrons as a function of their kinetic energy. *figure 2.9* shows the XPS spectrum of the $(2\bar{1}0)$ plane in Ga_3Ni_2 . It consists of a background signal, with several peaks overlaid. The tallest peaks correspond to photoelectron emission from certain atomic orbitals, but there are also peaks corresponding to *Auger electrons*.

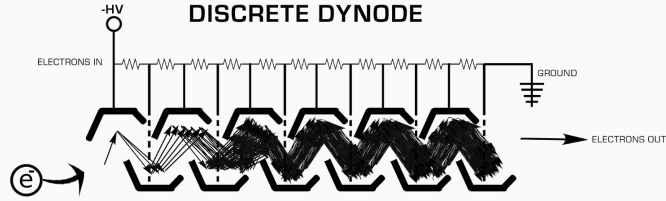


Figure 2.8: Discrete dynode schematic. The number of electrons emitted from a given dynode is always greater than the number which were incident, resulting in a multiplication of the signal at the detector.

The process of Auger emission occurs when an empty core level state in an atom is filled by an electron from a higher orbital. This transition is usually accompanied by the release of a photon, but sometimes the surplus energy can be transferred to a third electron, whose sub shell has sufficiently low binding energy for this newfound energy to induce its emission [13]. The kinetic energy of an Auger electron is independent of the frequency of the photon which caused the original core level emission, instead it is a function of the binding energies of the three states involved.

$$E_{k,photoemission} = h\nu - E_B - \phi$$

$$E_{k,Auger} = E_1 - E_2 - E_3 - \phi$$

E_1 is the binding energy of the vacant state generated by absorption of an x-ray photon. E_2 is the binding energy of the state an electron which fills the vacancy comes from. E_3 is the binding energy of the state the Auger electron is emitted from.

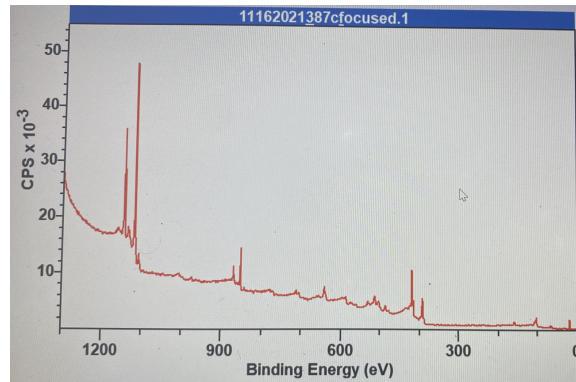


Figure 2.9: XPS spectrum of Ga_3Ni_2 ($2\bar{1}0$). CPS (y-axis) is counts per second; the number of electrons incident on the electron multiplier per second. By passing the parameters ν and ϕ to the computer, measured kinetic energies can be converted to binding energies (x-axis).

2.7.2 Methods of Analysis

XPS analysis in this project was done with the goal of determining the chemical composition at the material surface; the relative concentration of Gallium and Nickel atoms. The area of elemental peaks seen in XPS spectra is proportional to the number of photoelectrons emitted from the particular element, and the number of photoelectrons emitted from said particular element is proportional to its abundance at the surface. The process of XPS analysis therefore consisted of measuring the areas of particular elemental peaks, and then working back to determine the surface chemical composition.

The first step in this analysis was to index the peaks seen in XPS spectra, i.e. determine which element and sub shell peaks corresponded to. The binding energies of most elemental sub shells are tabulated, published values, and these can be found in *Appendix G: Summary of XPS Related Quantities*. Pairs of peaks appearing closely together correspond to emission from the same atomic sub shell, but energies have been split by *spin-orbit* coupling. Spin-orbit coupling occurs in sub shells with orbital angular momentum $l = 1$ or higher. Electrons can have intrinsic angular momentum $s = \frac{1}{2}$ or $s = -\frac{1}{2}$, and these two angular momenta couple to give total angular momentum $j = |l + s|$. In a 2p sub shell for example, $l = 1$ and j can take the values $\frac{1}{2}$ or $\frac{3}{2}$. The state with $j = \frac{1}{2}$ will have a slightly higher binding energy. This leads to the classification of 2p peaks as $2p_{\frac{1}{2}}$ and $2p_{\frac{3}{2}}$.

Next, peak areas were measured. This was done using CasaXPS [13]. *Figure 2.10* shows the calculation of a Ni $2p_{\frac{3}{2}}$ peak area in CasaXPS.

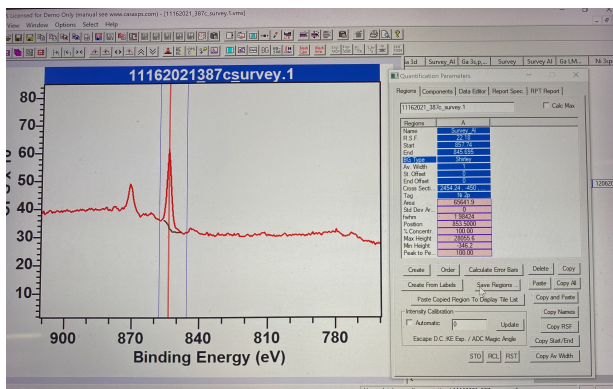


Figure 2.10: Calculation of a peak area. Blue lines are manually moved to the edges of the peak, and the counts in each channel between the lines summed. From this, the background is subtracted; this is the area beneath the brown line. Several background fit types can be used in CasaXPS, for this project the Shirley fit type was always used.

To find the concentration of a particular atom species at the surface, the peak areas of peaks from the same element must be summed together, and this sum divided by the sum of all peaks across all elements, giving a number between zero and one. One would mean that the entirety of the surface was composed of the element in question, while zero would mean there was none of said element at the surface, since no photoemission occurred from that element. However peak areas must first be normalised, since photoemission is not equally probable for all atom types. The probability of photoemission is dependent on the photoionisation cross section of the atom, the mean free path of the emitted electron, and

a whole host of other parameters. Handily, CasaXPS wraps all of these parameters up into a single factor, the *relative sensitivity factor*, or RSF (see *appendix F*). The process of peak area normalisation is therefore the process of dividing each peak area by its RSF.

Since Ga₃Ni₂ contains only two atom species, only two calculations must be performed in order to obtain the surface chemical composition; the concentration of Gallium atoms, and the concentration of Nickel atoms. Generalising this to binary materials, containing atoms of type A and atoms of type B, the equations are:

$$F(A) = \frac{\sum_{i=0}^n \left(\frac{Peak_i^A}{RSF_i^A} \right)}{\sum_{i=0}^n \left(\frac{Peak_i^A}{RSF_i^A} \right) + \sum_{i=0}^n \left(\frac{Peak_i^B}{RSF_i^B} \right)}$$

The numerator is a summation over all peaks i of the atom species A, and the denominator is a sum of two summations; one over all peaks i of the atom species A, and one over all peaks i of the atom species B.

$$F(B) = \frac{\sum_{i=0}^n \left(\frac{Peak_i^B}{RSF_i^B} \right)}{\sum_{i=0}^n \left(\frac{Peak_i^A}{RSF_i^A} \right) + \sum_{i=0}^n \left(\frac{Peak_i^B}{RSF_i^B} \right)}$$

Chapter 3

Results and Discussions

3.1 XPS Results

XPS data taken on the $(2\bar{1}0)$ plane of Ga_3Ni_2 , after annealing to different temperatures, was analysed to study the effect of annealing temperature on composition change. A graph showing the chemical composition of the surface as a function of different annealing temperatures is shown in *figure 3.1*:

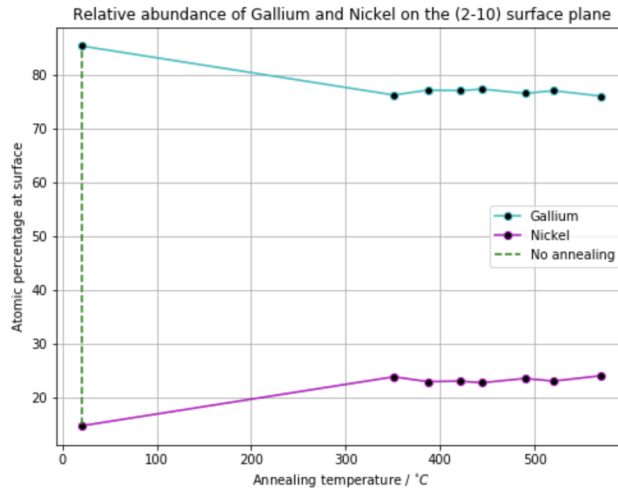


Figure 3.1: Plot of atomic percentages of Gallium and Nickel at the $(2\bar{1}0)$ surface. Datapoints on the dashed line correspond to a sample which was only sputtered and not annealed.

After only annealing has taken place, the surface is dominated by Gallium ($\approx 85\%$), however annealing leads to the composition changing, with the percentage of Gallium reducing, and that of Nickel increasing. This is the result of annealing promoting the diffusion of Nickel atoms to the surface.

The lack of datapoints at annealing temperatures below 351°C is due to the infrared sensor used to monitor the temperature of the sample during annealing proving unreliable at temperatures below $\approx 300^\circ\text{C}$. In future studies of Ga_3Ni_2 , a method of reading lower

temperatures should be employed, as this would allow the effect of annealing to be studied better. At 351°C and above, the composition has already 'levelled out', annealing at higher temperatures promotes no further change.

The annealing promotes diffusion of bulk atoms to the surface to fill vacancies, and so the diffusion of Nickel atoms to the surface which is seen indicates that vacancies on Nickel atom sites are the dominant vacancy which results from sputtering. Nickel atoms are *preferentially sputtered*.

Chapter 4

References

1. M. Wencka et al. The effect of surface oxidation on the catalytic properties of Ga_3Ni_2 intermetallic compound for carbon dioxide reduction, *Journal of Analytical Science and Technology*, June 2008.
2. Laurel Hamers, Explainer: What is a catalyst? *Science News for Students*, February 2017.
3. M. Wencka, M. Pillaca, P. Gille, Single crystal growth of Ga_3Ni_2 by the Czochralski method, *Journal of Crystal Growth*, 2016.
4. henniker scientific, <https://www.henniker-scientific.com/index.php/vacuum-and-uhv-surface-analysis/68>, accessed May 2022.
5. Vacuum Science World, <https://www.vacuumsceinceworld.com/ultra-and-extreme-high-vacuum>, accessed May 2022.
6. D. Agboola, U. Benson, Physisorption and Chemisorption Mechanisms Influencing Micro (Nano) Plastics-Organic Chemical Contaminants Interactions: A Review, Covenant University Nigeria, May 2021
7. Aglient Technologies, Aglient Ion Pumps Manual, 2016
https://web.archive.org/web/20160304090317/http://www.agilent.com/cs/library/catalogs/public/06_Ion_Pumps_Manual.pdf
8. E. Taglauer, Surface Cleaning Using Sputtering, *Applied Physics A - Solids and Surfaces*, 1990
9. H. Vic Dannon, Wave-Particle Duality: de Broglie Waves and Uncertainty, *Gauge Institute Journal* Vol. 2 No 4, November 2006
10. A.M. Glazer, The first paper by W.L. Bragg – what and when?, *Crystallography Reviews* Volume 19, 2013
11. <https://inkscape.org/>
12. I. Horcas, R. Fernández, J.M. Gómez-Rodríguez, J. Colchero, J. Gómez-Herrero and A.M. Baró, *Review of Scientific Instruments* 78, 013705 (2007)

13. IUPAC. Compendium of Chemical Terminology, 2nd ed. (the "Gold Book"). Compiled by A. D. McNaught and A. Wilkinson. Blackwell Scientific Publications, Oxford (1997). Online version (2019-) created by S. J. Chalk. ISBN 0-9678550-9-8. <https://doi.org/10.1351/goldbook>
14. <http://www.casaxps.com/>

Chapter 5

Appendices

5.1 Appendix A: Bravais Lattices

The fourteen possible three dimensional Bravais lattices are shown below:

Bravais lattice	Parameters	Simple (P)	Volume centered (I)	Base centered (C)	Face centered (F)
Triclinic	$a_1 \neq a_2 \neq a_3$ $\alpha_{12} \neq \alpha_{23} \neq \alpha_{31}$				
Monoclinic	$a_1 \neq a_2 \neq a_3$ $\alpha_{23} = \alpha_{31} = 90^\circ$ $\alpha_{12} \neq 90^\circ$				
Orthorhombic	$a_1 \neq a_2 \neq a_3$ $\alpha_{12} = \alpha_{23} = \alpha_{31} = 90^\circ$				
Tetragonal	$a_1 = a_2 \neq a_3$ $\alpha_{12} = \alpha_{23} = \alpha_{31} = 90^\circ$				
Trigonal	$a_1 = a_2 = a_3$ $\alpha_{12} = \alpha_{23} = \alpha_{31} < 120^\circ$				
Cubic	$a_1 = a_2 = a_3$ $\alpha_{12} = \alpha_{23} = \alpha_{31} = 90^\circ$				
Hexagonal	$a_1 = a_2 \neq a_3$ $\alpha_{12} = 120^\circ$ $\alpha_{23} = \alpha_{31} = 90^\circ$				

Figure 5.1: Bravais lattice unit cells. a_i are lattice parameters, whilst α_{ij} are the angles between them.

5.2 Appendix B: Calculation of Miller Indices

For any real space lattice, there are an infinite number of possible planes which intersect the lattice, each with a unique set of Miller indices (**hkl**). The integers h, k and l relate to positions on the x, y and z coordinate axes respectively. The process for calculating these proceeds as follows:

1. Find the intercepts of the plane with each of the coordinate axes; for example in the illustration below these intercepts are at $x = 2$, $y = 4$ and $z = 3$.
2. Take the reciprocals of these intercepts: 2, 4 and 3 become $\frac{1}{2}$, $\frac{1}{4}$ and $\frac{1}{3}$.
3. Multiply these reciprocals by the *smallest number* which will clear the fractions (i.e. make all values integers). In the case shown below, the smallest integer is 12, and so $h = \frac{1}{2} \times 12 = 6$, $k = \frac{1}{4} \times 12 = 3$, and $l = \frac{1}{3} \times 12 = 4$. Therefore for the plane in the illustration below, $(hkl) = (6, 3, 4)$.

Negative miller indices are denoted with a bar, rather than a minus sign in front of the index. For example, if a plane intersected the x, y and z axes at 1, -1 and 0 respectively, its Miller indices would be expressed as $(1, \bar{1}, 0)$.

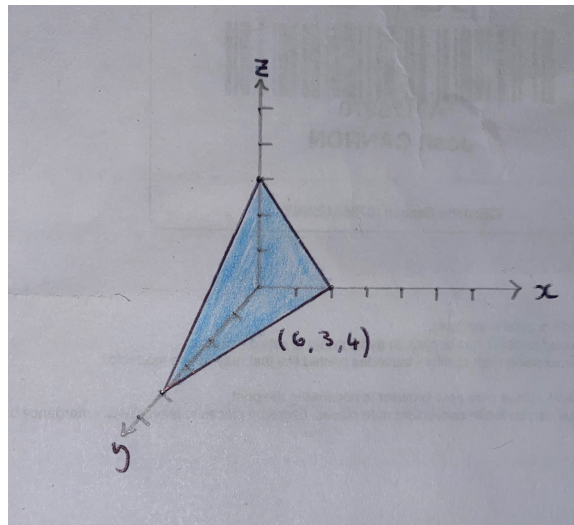


Figure 5.2: Real space plane with Miller indices 6, 3, 4

5.3 Appendix C: Bulk Plane Structures

The structures of four different surface planes were studied in this experiment: (100), (010), (001) and $(2\bar{1}0)$. The bulk structures of these planes, modelled in VESTA, are shown in the following figures:

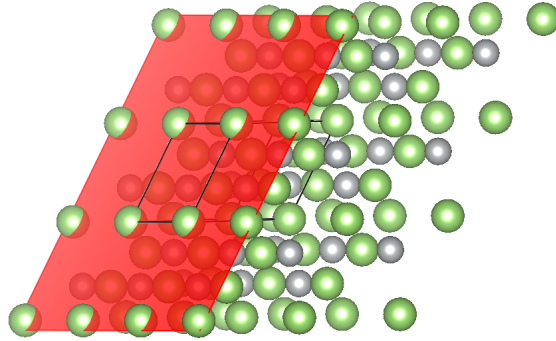


Figure 5.3: (100)

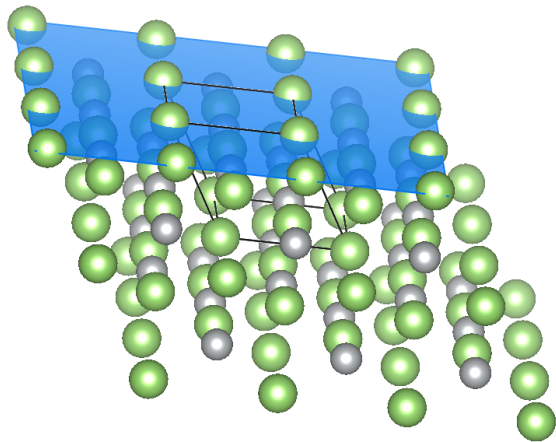


Figure 5.4: (010)

5.4 Appendix D: Physical Principles of Vacuum Pumps

Rotary pumps use a rotating vane of variable length, and therefore variable volume. (See illustration below). When the end of this vane is aligned with the inlet to the vacuum system, its volume expands, reducing the internal pressure and pulling in gas from the chamber (position 1). As rotation continues, the vane is separated from the chamber (position 2). Further rotation compresses the internal volume of the vane, increasing pressure, and as the end of the vane passes the outlet gas molecules are expelled. A valve at the outlet discourages back flow of gases into the vane.

Sorption pumps rely on adsorption of gas molecules to porous materials such as Zeolite, which have large surface area : volume ratios to maximise this process. The inlet is opened, gas molecules are adsorbed, then the inlet is closed and an outlet is opened, molecules can then desorb from the Zeolite and pass through, allowing the process to be repeated.

Turbomolecular pumps employ rotor - stator pairs, with blades inclined in opposite

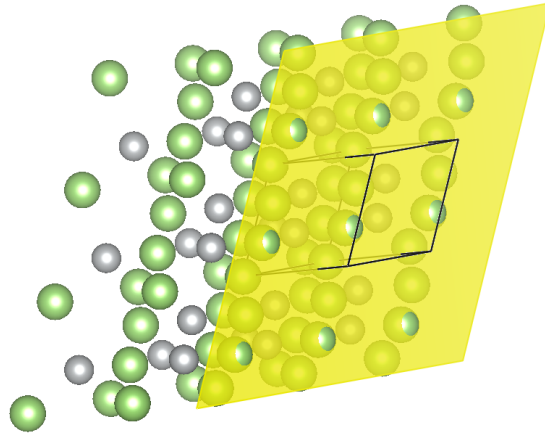


Figure 5.5: (001)

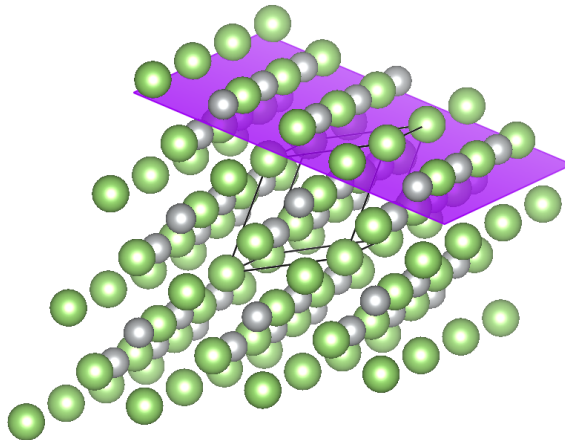


Figure 5.6: (2 $\bar{1}$ 0)

directions. The rotors spin at 15 000 - 30 000 rpm, and transfer momentum to gas molecules, which are directed to the stator below. Another rotor - stator pair below this drives molecules down further. This is repeated all the way down the pump structure, resulting in molecules being drawn away from the vacuum system. A roughening pump is connected to the outlet.

Diffusion pumps use downward-flowing jets of hot oil to physically push gas molecules towards an outlet. Pumping oil is heated, rises up a central column, and then is then directed downwards. The downward flows collide with gas molecules in the vacuum, pushing them downwards to the bottom of the pump and thus raising the pressure in this region. A backing pump then draws them out.

Ion pumps feature an anode and a cathode, held at such a high potential that electrons

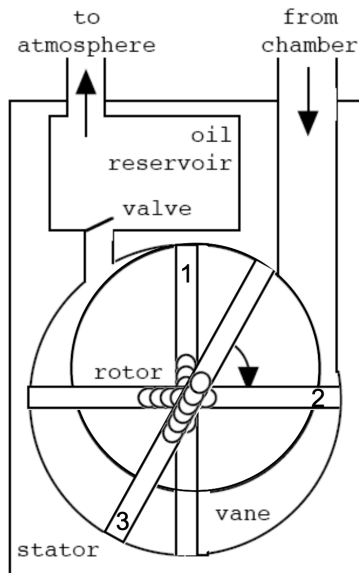


Figure 5.7: Rotary pump schematic

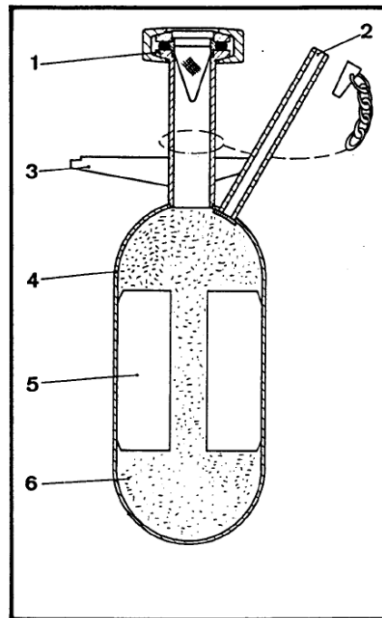


Figure 5.8: Sorption pump schematic. 1: Inlet. 2: Outlet. 3: Support. 4: Body. 5: Thermal conducting vanes. 6: Zeolite

are emitted from the cathode. When these electrons collide with gas molecules they can knock off orbital electrons, ionising the molecules and causing them to be pulled to the cath-

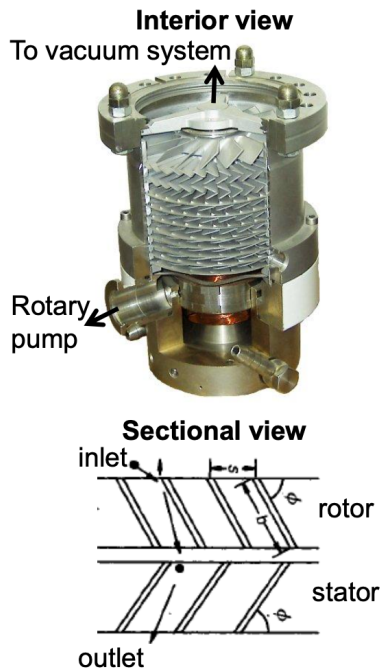


Figure 5.9: Top: cutaway image showing the internal structure of a turbomolecular pump. Bottom: diagram of a rotor - stator pair.

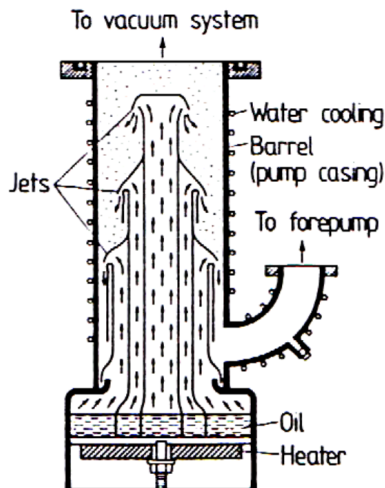


Figure 5.10: Diffusion pump schematic

ode, where they are captured. A magnetic field in the region between the electrodes causes electrons to follow a helical path, increasing the path length and therefore the probability of collision with a gas molecule. An ion pumping system is made more effective by increasing the number of anode-cathode cells.

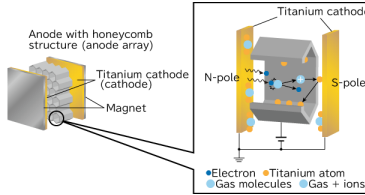


Figure 5.11: Ion pump schematic

Cryo pumps use liquid helium to condense gas molecules to the liquid phase in order to remove them from the vacuum system. They are not very common.

5.5 Appendix E: The Piezoelectric Effect

Certain materials with a crystalline structure can exhibit the phenomenon of piezoelectricity. This is the generation of a potential difference between two opposing faces of the crystal, when the crystal is compressed. If a conducting material is used to connect the two sides to one another, then this potential difference can cause a current to flow.

A schematic of this is shown in the figure below. In **(a)**, electric dipoles are randomly oriented, and the net electric field is zero. In **(b)**, stress (pressure) is applied to the top and bottom of the crystal, and strain (compression) occurs. This increases the alignment of the electric dipoles, resulting in a net electric field pointing from the bottom to the top. This means there is an electric potential difference between the top and bottom of the crystal, i.e. a voltage, which can be used to drive a current. **(c)** shows the corollary to this; applying a voltage across the crystal causes increased alignment of the electric dipoles, and compression of the material.

Note that compression / extension of a material in one axis will result in the opposite in the perpendicular axes. The extent of this is quantified by *Poisson's ratio* ν , the ratio of transverse / axial strain in a material under stress. (Axial strain is strain parallel to the direction of the applied force, transverse strain is strain perpendicular to the direction of applied force).

$$\nu = \frac{d\epsilon_{trans}}{d\epsilon_{axial}}$$

It is the voltage-induced compression of crystals which is exploited for atomic-level precision in STM tip movement, as applying electric fields to a piezoelectric crystal results in minuscule changes in size. By stacking multiple piezoelectric units on top of one another, and having one end of the stack affixed to an immovable mount and the other end connected to the STM tip, the position of the STM tip can be moderated very finely along the stacking axis. This allows the tip to be moved in steps as small as individual atoms.

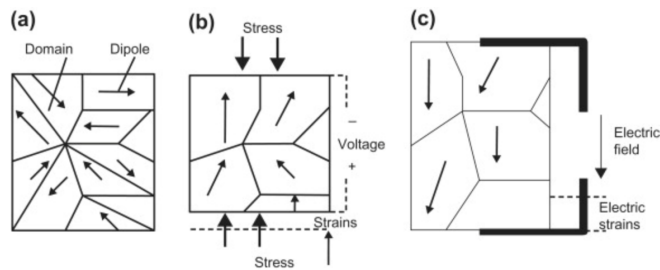


Figure 5.12: Illustration of the piezoelectric effect

Source	Energy/eV	Line Width/eV
Al	1253.6	0.7
Mg	1486.6	0.85

5.6 Appendix F: K_{α} X-ray Sources

5.7 Appendix G: Summary of XPS Related Quantities

Element	Subshell	Binding Energy/eV	X-ray Energy/eV	RSF
Ni	2s	987.3	0.071	5.16
	2p	868.8	0.2998	22.18
	3s	116.6	0.012	22.18
	3p	78.3	0.029	1
	4s	7.9	0.00083	1
	3d	15.2	0.0059	1
Ga	2s	1260.4	0.083	1
	2p	1124.2	0.4412	32.49
	3s	152.9	0.015	32.49
	3p	107.4	0.043	1
	4s	11.4	0.0012	1
	3d	27.8	0.014	1